PAPER

Check for updates

Harnessing the unusually strong improvement of thermoelectric performance of AgInTe₂ with nanostructuring†

Jose J. Plata, [iD] *[a] Ernesto J. Blancas, [iD] [a] Antonio M. Márquez, [iD] [a] Victor Posligua, [iD] [b] Javier Fdez Sanz[a] and Ricardo Grau-Crespo [iD] [c]

Nanostructuring is a well-established approach to improve the thermoelectric behavior of materials. However, its effectiveness is restricted if excessively small particle sizes are necessary to considerably decrease the lattice thermal conductivity. Furthermore, if the electrical conductivity is unfavorably affected by the nanostructuring, it could cancel out the advantages of this approach. Computer simulations predict that silver indium telluride, $AgInTe_2$, is unique among chalcopyrite-structured chalcogenides in requiring only a mild reduction of particle size to achieve a substantial reduction in lattice thermal conductivity. Here, *ab initio* calculations and machine learning are combined to systematically chart the thermoelectric properties of nanostructured $AgInTe_2$, in comparison with its Cu-based counterpart, $CuInTe_2$. In addition to temperature and doping carrier concentration dependence, ZT is calculated for both materials as functions of the polycrystalline average grain size, taking into account the effect of nanostructuring on both phonon and electron transport. It is shown that the different order of magnitude between the mean free path of electrons and phonons disentangles the connection between the power factor and lattice thermal conductivity when reducing the crystal size. ZT values up to 2 are predicted for p-type $AgInTe_2$ at 700 K when the average grain size is in the affordable 10–100 nm range.

1. Introduction

The recovery of heat as electricity through the use of thermoelectric (TE) materials has attracted the attention of researchers since the Seebeck and Peltier effects were described at the beginning of the 19th century. The increasing global energy demand and the high volatility of the oil and gas markets, together with the fact that 70% of energy produced by our society is wasted as heat, makes the development of thermoelectric materials a pressing societal need. The discovery of more efficient and economical thermoelectric materials remains a challenging task, as does the optimization of existing thermoelectric materials. In recent decades, significant resources have been dedicated to the improvement of the performance of these materials,[1] measured by its figure of merit, $ZT = S^2\sigma T/(\kappa_{elec} + \kappa_{latt})$, where σ is the electrical conductivity, κ_{elec} and κ_{latt} are the electrical and lattice thermal conductivities respectively, T is the temperature and S is the Seebeck coefficient. Maximizing ZT is a complex task,

as these materials properties are strongly coupled.[2] Additionally, the difficulty of establishing robust connections between real-space synthetic variables (temperature, chemical composition, doping concentration or grain size) and reciprocal-space materials properties that modify ZT (scattering times or electronic and vibrational structure) hampers the discovery of new and more efficient thermoelectric materials.

Computational materials science has changed this paradigm in the 21st century with the development of methodologies and frameworks to accurately calculate transport properties[3–7] and analyze the effect of some variables such as their chemical composition.[8] However, predicting the TE performance of bulk single crystal materials through computational screening[9] does not guarantee a high efficiency in the final device. TE performance of materials is drastically modified by some variables linked to processing, such as doping concentration or grain size, so candidate materials need to go through an optimization process. Although many strategies such as alloying,[10] doping,[11] dislocation,[12] or phase engineering[13,14] have been proposed to enlarge and optimize ZT, they often involve laborious and time-consuming repeated experiments of synthesis, characterization and property measurement. One of the most common strategies is the nanostructuring or nanocrystalization, which was proposed for the first time by Dresselhaus in the 1990s.[15] Tailoring the grain size in polycrystalline samples has led to significant improvements of the thermoelectric performance of

[a]Departamento de Química Física, Universidad de Sevilla, Seville, Spain. E-mail: jplata@us.es

[b]Department of Chemistry, Imperial College London, Molecular Sciences Research Hub, London, UK

[c]Department of Chemistry, University of Reading, Reading, UK

16734 | *J. Mater. Chem. A*, 2023, 11, 16734–16742

This journal is © The Royal Society of Chemistry 2023

materials.[16,17] For instance, controlling the nanostructure of half-Heusler alloys leads to an enhancement of their power factor, PF $= S^2\sigma$.[18] However, the critical reduction of κ_{latt} plays the dominant role, increasing ZT when grain size is reduced to the nanoscale.[19]

The effect of the grain size on κ_{latt} mainly depends on the phonon lifetimes, which can present different behaviors even in a set of materials with the same structural prototype. In previous work,[20] we reported that the grain size, $L_{0.5}$, needed to halve the lattice thermal conductivity κ_{latt} across a family of chalcopyrite semiconductors was roughly proportional to the bulk thermal conductivity value (Fig. 1). Considering that trend, $AgInTe_2$ can be identified as an outlier, with an unusual potential to benefit from nanostructuring, in the sense that its κ_{latt} can be reduced to half of its bulk value with a substantially less drastic reduction of grain size, if compared to other Se- and Te-based chalcopyrites with similar bulk conductivities. $AgInTe_2$, $CuInTe_2$ and their alloys have been extensively studied during recent years due to their promising thermoelectric performance. ZT values above 1.5 have been measured for $CuInTe_2$ by domain engineering[21] or manipulating localized vibrations of interstitial Te atoms.[22] Despite these outstanding values, there is a large variability on the reported figures of merit of these materials due to the strong dependence of this parameter with the chemical nature of the monovalent cation, temperature, carrier concentration and grain size or nano-structure. Here, we present, for first time, a theoretical approach to accurately and systematically explore the multi-variate space that defines the TE performance of $CuInTe_2$ and $AgInTe_2$, paying special attention to the role of the grain size in polycrystalline samples and opening the door to perform *in silico* optimization of TE materials.

2. Methodology

2.1 Geometry optimization

$CuInTe_2$ and $AgInTe_2$ chalcopyrite structure were fully relaxed (atoms and lattice) with the VASP package,[23,24] using projector-augmented wave (PAW) potentials.[25] Energies were obtained using the exchange–correlation functional proposed by Perdew–Burke–Ernzerhof (PBE),[26] including Grimme-D3 van der Waals corrections.[27] Core and valence electrons were selected following standards proposed by Calderon *et al.*[28] An accurate description of the minimum of the potential energy surface was obtained using a high-energy cut-off of 500 eV and a dense mesh of 4096 *k*-points per reciprocal atom. Geometry and lattice vectors were fully relaxed, using a 16-atom conventional cell, until forces acting over each atom were smaller than 10^{-7} eV $\mathring{A}^{-1}$. Wave-function was considered converged when the energy difference between two consecutive electronic steps was smaller than 10^{-9} eV, including an additional support grid for the evaluation of the augmentation charges to reduce the noise in the forces.

2.2 Supercell single-point calculations and force constants

HiPhive package was used to calculate interatomic force constants, IFCs, combining the forces calculated for random atomic distortions in supercells with machine learning regression.[29,30] The forces were calculated in 18 $4 \times 4 \times 2$ supercells (512 atoms) using the same setup as the one used for geometry optimizations. A Monte Carlo algorithm was used to set the amplitude of the distortions applied to each atom, obtaining an average displacement amplitude for each configuration of $\sim$0.13 Å. The force constants were extracted from a multi-linear regression of the DFT forces, applying the recursive feature elimination, RFE, algorithm. Reducing the number of parameters *via* RFE also simplifies the model, keeping only the most relevant interaction terms. IFCs were calculated including cutoffs for second, third and fourth-order terms, following the same strategy as in previous work.[20]

2.3 Boltzmann transport equation solver

The ShengBTE code is used in order to solve the Boltzmann transport equation, BTE, for phonons and calculate the lattice thermal conductivity, κ_{latt}.[31] Scattering times were computed including isotopic and three-phonon scattering effects. Memory demand and the convergence of κ_{latt} with the number of *q*-points were balanced using a Gaussian smearing of 0.1 and a dense mesh of $20 \times 20 \times 10$ *q*-points. The value of κ_{latt} for polycrystalline samples with an average grain size of L is approximated as the cumulative contributions from all mean free paths up to L. This strategy has led to a good description of the lattice thermal conductivity of $CuGaTe_2$ and other chalcopyrites.[20]

2.4 Electronic transport properties

Electrical conductivity, σ, Seebeck coefficient, S and the electronic contribution to the thermal conductivity, κ_{elec} were calculated using the AMSET package.[3] This code solves the electronic BTE using the Onsager coefficients to predict electronic transport properties with the wavefunction from a DFT calculation as main input. Scattering rate for each temperature, doping concentration, band, and *k*-point are calculated including scattering due to deformation potentials, ADPs,
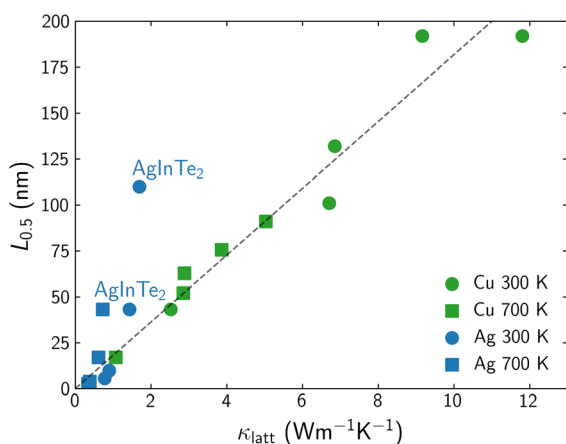

Fig. 1 Correlation between $L_{0.5}$ and bulk κ_{latt} for Cu- (green) and Ag-based (blue) chalcopyrites at 300 K (circles) and 700 K (squares). $AgInTe_2$ outlayer is labeled. Adapted from Plata *et al.*[20]

This journal is © The Royal Society of Chemistry 2023

J. Mater. Chem. A, 2023, **11**, 16734–16742 | **16735**

piezoelectric interactions, PIEs, polar optical phonons, POPs, and ionized impurities, IMPs. Electronic transport properties were calculated using the primitive cell (8 atoms) and a dense mesh of $10 \times 10 \times 10$ k-points. Polar phonon frequency and elastic constants were calculated using the same setup described previously. Wave-function coefficients and deformation potential were calculated using the HSE06 [32,33] functional in order to obtain an accurate description of the electronic structure. Static dielectric constants were calculated as the sum of the high-frequency dielectric constants and the ionic dielectric constants. Ionic dielectric constants were calculated using density functional perturbation theory.[34,35] Due to the strong dependence of the high-frequency dielectric constant with the band gap and thus with the exchange–correlation functional, experimental values reported by Holah[36] and Kumar[37] were used. Electron scattering at grain boundaries was included as v_g/L where v_g is the group velocity and L the mean free path.

3. Results

The optimization of the TE performance of AgInTe$_2$ and CuInTe$_2$ is performed based on three main variables: temperature, T, carrier concentration, n, and average grain size, L, which can be modified during the synthesis or TE module operation. CuInTe$_2$ and most TE efficient chalcopyrites have been reported as p-type materials; however, AgInTe$_2$ has been described both as p-type and n-type, depending on the crystal growth conditions.[38] For this reason, CuInTe$_2$ is explored as a p-type semiconductor, while the TE performance of AgInTe$_2$ is calculated for both p- and n-type carriers.

There is very limited information in the literature about the electronic transport properties of AgInTe$_2$, but there are many previous experimental studies of CuInTe$_2$, which therefore will be used to validate our theoretical framework. Electrical conductivity, σ, and Seebeck coefficient, S, are explored in a wide range of temperatures ($T = 300–700$ K) and carrier concentrations ($n = 10^{17}–10^{20}$ cm^{-3}). The carrier concentration range has been selected based on the previously reported experimental values for CuInTe$_2$, which is wider than the range for AgInTe$_2$. At 300 K, calculated σ and S present a reasonably good agreement with available experimental data[39–48] (Fig. 2). While σ is slightly underestimated at low and medium carrier concentrations (Fig. 2a), S is slightly overestimated (10–15% error) in the whole range of concentrations (Fig. 2b). These deviations cancel each other when the power factor, PF = $S^2\sigma$, is calculated, with PF deviations being significant only when $n > 2 \times 10^{19}$ cm^{-3} (Fig. 2c). Putting these discrepancies in context, we note that they are similar to the experimental uncertainty in electric transport measurements. For example, the analysis by Mackey *et al.*[49] of the uncertainty in the measurement of electronic thermoelectric properties based on the four-probe method, found that electrical resistivity measurements contain a 7% uncertainty across any temperature, Seebeck coefficient measurements presents between 1% and 13% uncertainty depending on the temperature, and the power factor has a combined uncertainty of +7.3%/−27%. In addition to the uncertainty on the experimental measurements, part of
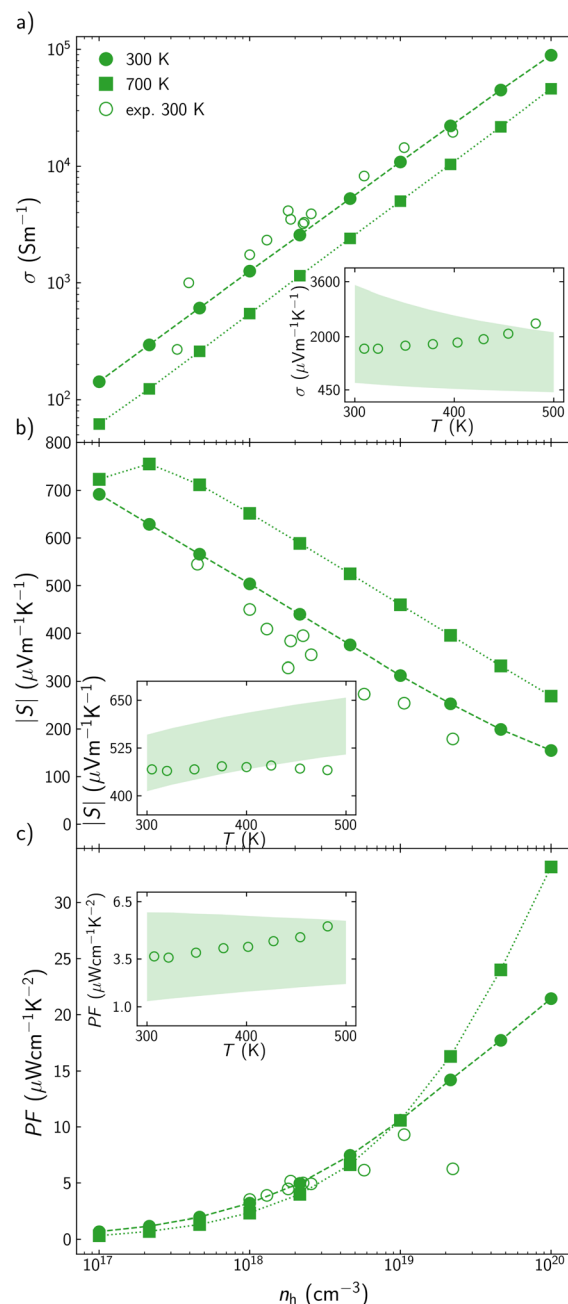

Fig. 2 (a) Electrical conductivity, σ, (b) Seebeck coefficient, S, and (c) power factor, PF, for CuInTe$_2$ at different hole concentration, n_h, at 300 K (circles) and 700 K (squares). Reported experimental data are represented with empty points.[39–48] Inset figures show σ, S, and PF at the 300–500 K interval. Shading area is enclosed by the calculated values using the minimum and maximum experimental carrier concentrations reported for that temperature range.[47]

the discrepancies between calculated and experimental values stem from scattering processes at the point defects created when reaching such high carrier concentrations, which are not included in our theoretical model. In the AMSET code, comparing theoretical predictions and experimental results based on how σ and S change with temperature present some challenges. Carrier concentration increases when temperature

16736 | *J. Mater. Chem. A*, 2023, **11**, 16734–16742

This journal is © The Royal Society of Chemistry 2023

is increased, so experimentally, both variables change simultaneously. Based on previous studies,[47] σ and S have been computed at two different carrier concentrations that would be the upper and lower limits experimentally reported for a specific temperature range. While all experimental σ values between 300 and 500 K are in between the calculated upper and lower limits (inset in Fig. 2a), some of the calculated S at higher temperatures are slightly overestimated, around 7% error (inset in Fig. 2b). When calculated σ and S are combined in the PF, this is

in a very good agreement with data for the whole range of temperatures. Experimental PF around 300 K is very close to the calculated lower limit ($n = 5 \times 10^{17}$ cm^{-3}).[47] The carrier concentration increases when temperature is raised so experimental PF values close to 500 K are similar to the calculated values, using the upper carrier concentration limit ($n = 3 \times 10^{18}$ cm^{-3}). Overall, the proposed theoretical framework predicts the behavior of the electronic transport properties with a higher accuracy than other approaches. For instance, Wei et al. predicted $\sigma = 3.85 \times 10^4$ S m^{-1} at 300 K and $n = 2.69 \times 10^{19}$ cm^{-3} which is approximately a 100% error with respect to experimental values.[50]

AgInTe$_2$ presents slightly lower σ values than CuInTe$_2$ as p-type semiconductor but around one order of magnitude higher as n-type semiconductor (Fig. 3a). Due to Pisarenko relation, this trend is reverted for S, where p-type AgInTe$_2$ presents higher values than its n-type counterpart (Fig. 3b). These values can be hardly compared with experimental data because most studies did not or could not quantify the carrier concentration of the samples. This fact is in agreement with the extremely low carrier concentration observed in some reports, most of the time below 10^{17} cm^{-3}.[51] However, the experimental S reported by Wang et al. at 700 K[46] is in very good agreement with our predictions. Based on these results, it can be concluded that the lower PF observed for AgInTe$_2$ with respect
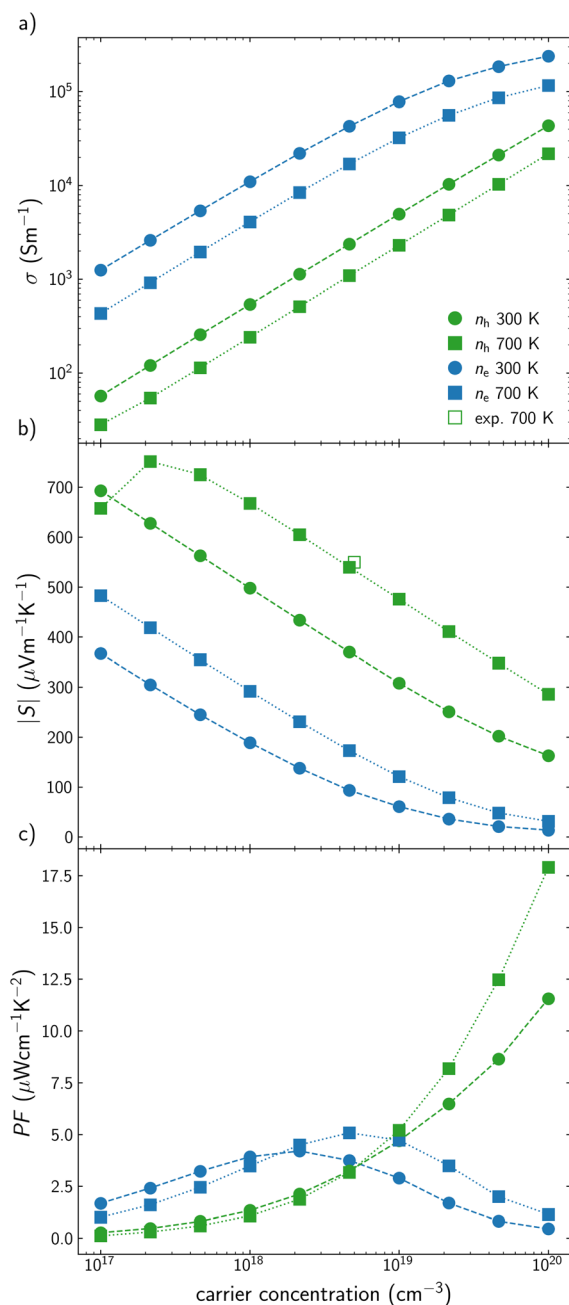

Fig. 3 (a) Electrical conductivity, σ, (b) Seebeck coefficient, S, and (c) power factor, PF, for AgInTe$_2$ at different carrier concentration, n, at 300 K (circles) and 700 K (squares). Green and blue are used for p-type and n-type conduction, respectively. Reported experimental data[46] are represented with empty points.
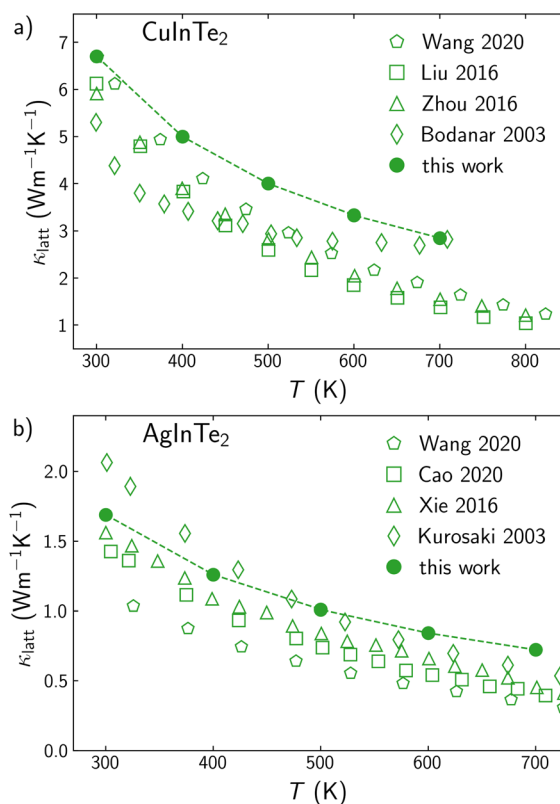

Fig. 4 Temperature variation of lattice thermal conductivity, κ_{latt}, for (a) CuInTe$_2$ and (b) AgInTe$_2$. Calculated values are represented with filled points while experimental values are depicted with empty points.[46,47,52–54]

This journal is © The Royal Society of Chemistry 2023

J. Mater. Chem. A, 2023, 11, 16734–16742 | 16737

to CuInTe$_2$ as p-type semiconductor stems from the lower carrier concentration of the material and not because of their electronic transport properties by themselves (Fig. 3c). Moreover, n-type AgInTe$_2$ presents higher PF than its p-type counterpart at low and medium carrier concentration values, being more accessible from a synthetic point of view (Fig. 3c).

At low carrier concentrations, the semiconductor nature of CuInTe$_2$ and AgInTe$_2$ makes the lattice thermal conductivity, κ_{latt}, the main contributor to κ in the whole range of explored temperatures. Comparing κ_{latt} obtained through the solution of the BTE with experiment is always a challenging task. Experimental samples are usually polycrystalline, which reduces the κ_{latt} due to the phonon scattering processes at the grain boundaries. Additionally, the defects connected to carriers (holes or electrons) also act as phonon scattering centers, reducing κ_{latt}. For instance, Yan et al. and Liu et al. have synthesized polycrystalline CuInTe$_2$ samples with similar micro-metric size but different carrier concentration at 300 K, 1.8×10^{18} cm^{-3} and 1.06×10^{19} cm^{-3}, respectively. The samples with higher carrier concentration (and point defects) present values for κ_{latt} around a 10% lower than the sample with lower carrier concentration. Our theoretical model does not explicitly include grain boundaries or point defects when

calculating bulk κ_{latt}, which is why our calculated values slightly overestimate experimental results (Fig. 4a). This overestimation is larger at high temperatures because (i) carrier concentration and point defects are increased with temperatures and (ii) 4th-order scattering processes contribute to κ_{latt} but are not included in the solution of the BTE.[55,56] Although a similar trend was found for AgInTe$_2$, the overestimation of the calculated values is considerably lower if compared with the CuInTe$_2$ results (Fig. 4b). This is partially due to the more than three times lower κ_{latt} found for AgInTe$_2$ with respect to CuInTe$_2$.

The improvement of ZT by fine-tuning the carrier concentration is hampered by physical laws that interconnect TE properties. For instance, Pisarenko plots show how there are limitations in the enlargement of S and σ simultaneously. Nanostructuring introduces a new variable, length scale, that permits the decoupling of the properties that govern thermoelectricity. The effect of the average grain size of a polycrystalline sample, L, on the transport properties of CuInTe$_2$ and AgInTe$_2$ is included in Fig. 5. Due to the low influence of L on S, we will focus on analyzing the behavior of PF and κ_{latt}, using two different temperatures (300 and 700 K) and a moderate carrier concentration of 4.64×10^{18} cm^{-3}. PF of p-type CuInTe$_2$ is reduced around a 5% when L is below 100 nm and between 25% and 32% when L is below 10 nm
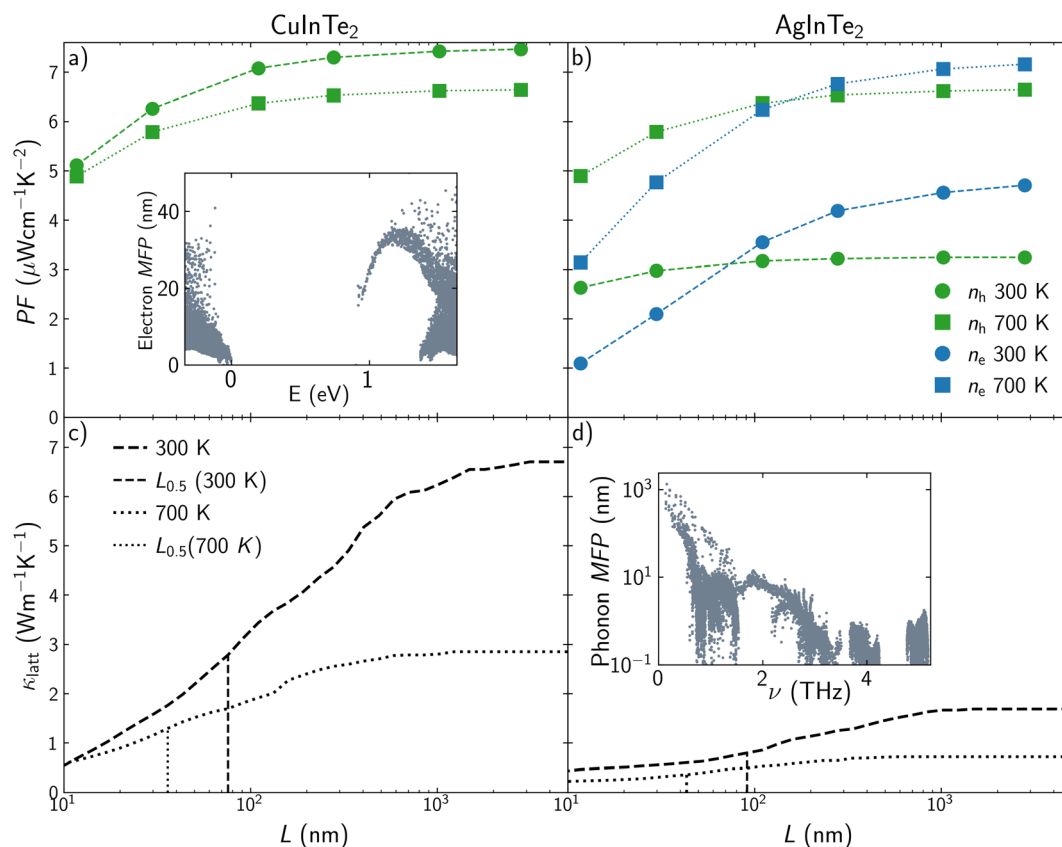

Fig. 5 Power factor, PF, dependence with the grain average size for (a) CuInTe$_2$ and (b) AgInTe$_2$ at $n = 4.64 \times 10^{18}$ cm^{-3}. Circles and squares are used for 300 K and 700 K, respectively. Green and blue colors are used for p-type and n-type semiconductors, respectively. The inset in panel (a) shows the electron mean free path, MFP, for p-type CuInTe$_2$ at 300 K. Lattice thermal conductivity, κ_{latt}, dependence with the grain size for (c) CuInTe$_2$ and (d) AgInTe$_2$ at 300 K (dashed line) and 700 K (dotted line). Vertical lines represent the grain size, $L_{0.5}$, in which κ_{latt} have been reduced a 50% with respect to the single crystal value. The inset in panel (d) shows the phonon mean free path, MFP, for p-type AgInTe$_2$ at 300 K.

16738 | J. Mater. Chem. A, 2023, 11, 16734–16742

This journal is © The Royal Society of Chemistry 2023

depending on the temperature (Fig. 5a). This trend is similar for p-type AgInTe$_2$, where PF is reduced around 2% when L is below 100 nm and between 15% and 25% when L is below 10 nm (Fig. 5b). The reduction of PF with L for n-type AgInTe$_2$ is slightly different, decreasing around 10% when L is below 100 nm and between 50% and 80% when L is below 10 nm (Fig. 5b). These results should be analyzed based on the mean free path, MFP, of the carriers (see inset in Fig. 5a). Valence band MFPs for CuInTe$_2$ are mostly below 40 nm at 300 K which explains the low reduction of PF above 100 nm. MFP values for AgInTe$_2$ valence band are even lower at 300 K so PF is only effectively reduced below 20 nm. However, n-type AgInTe$_2$ presents a more drastic reduction of PF when grain size is below 400 nm because conduction band MFP values are considerably larger for both CuInTe$_2$ and AgInTe$_2$ than the valence band MFP values. Lattice thermal

conductivity seems to be more sensitive to nanostructuring than PF (Fig. 5c and d). Both CuInTe$_2$ and AgInTe$_2$ present an approximate 50% reduction on κ_{latt} around 100 nm at 300 K. Unfortunately, κ_{latt} tuning at 700 K requires smaller grain sizes, with $L_{0.5}$ values around 30–40 nm. The drastic modification of κ_{latt} when average grain size is reduced from few micrometers to 100 nm is considerably larger than the κ_{latt} reduction experimentally observed by doping and discussed in the previous section, which confirms that grain boundary effects are the main cause of departure from ideal bulk behavior.

Similarly to holes and electrons, phonon MFP is the property governing this behavior. The most important contributions to κ_{latt} stem from acoustic and low-frequency optical modes (Fig. S2†), so examining their MFPs values is the key to understand the thermal conductivity behavior. The MFPs of acoustic
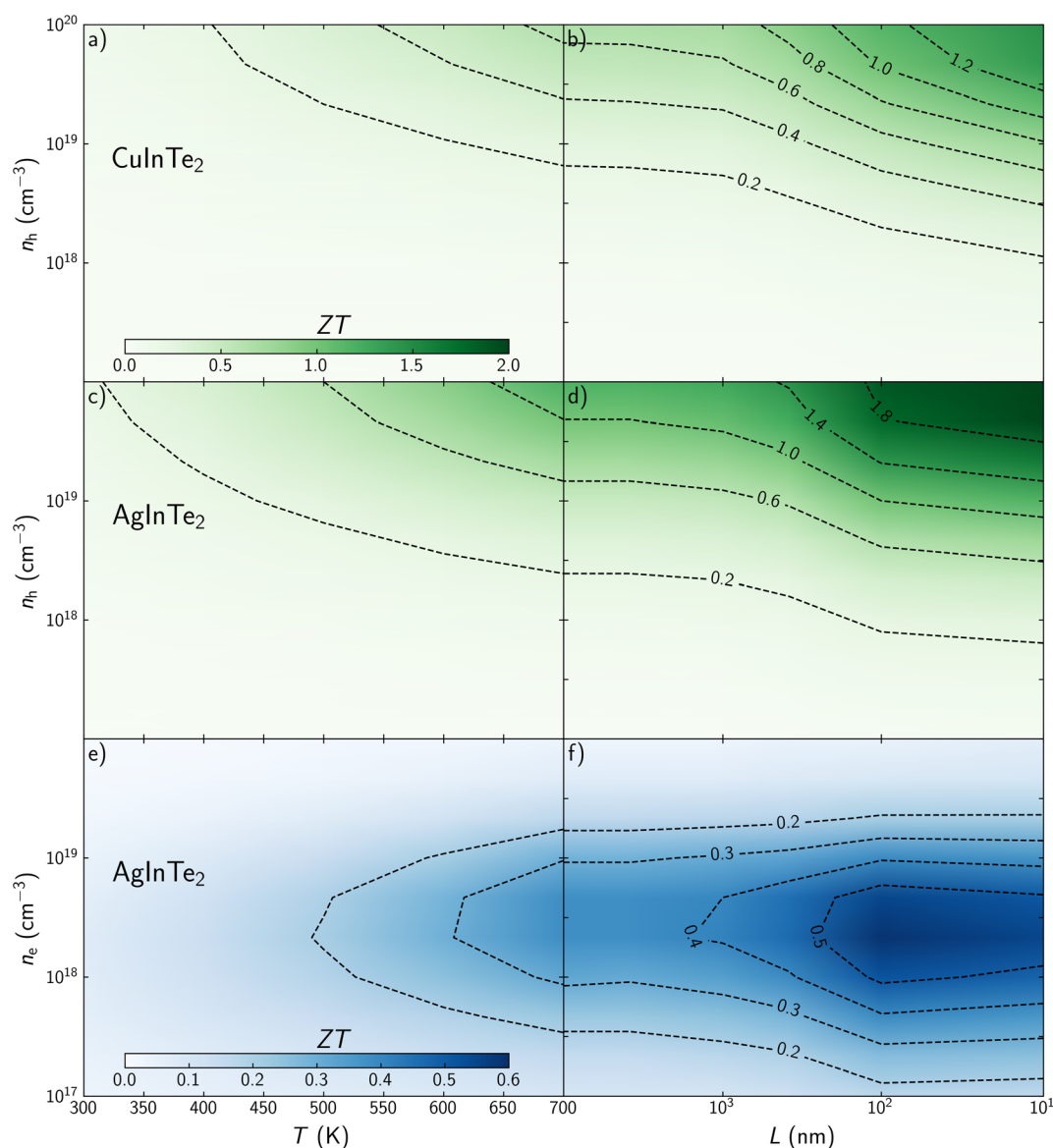

Fig. 6 Thermoelectric figure of merit, ZT, dependence on temperature, T, and carrier concentration, n for (a) p-type CuInTe$_2$, (c) p-type AgInTe$_2$ and (e) n-type AgInTe$_2$ single crystals. ZT dependence on average grain size, L, and carrier concentration, n for (b) p-type CuInTe$_2$, (d) p-type AgInTe$_2$ and (f) n-type AgInTe$_2$ polycrystalline samples at 700 K.

This journal is © The Royal Society of Chemistry 2023

J. Mater. Chem. A, 2023, **11**, 16734–16742 | **16739**

modes around Γ are larger for $CuInTe_2$ than for $AgInTe_2$, which is why κ_{latt} for $CuInTe_2$ is reduced even with large grain size above 1 μm (see inset at Fig. 5d). However, MFP values for both materials are moderately high in the range of 0–1 THz so their κ_{latt} drastically decrease when particle size is reduced in the range of 1 μm–100 nm. The origin of these large MFP is linked to the high group velocities and low scattering rates of the acoustic modes (Fig. S2†). This behavior is less pronounced at high temperatures where scattering times and MFPs are shorter.

Once electronic and phonon transport properties have been predicted, the thermoelectric figure of merit, ZT, can be studied considering temperature, carrier concentration and grain size as main variables. Contour plot – heat maps shows how ZT increases with temperature in the explored range for both materials (Fig. 6a, c and e). This is not the case for carrier concentration. While ZT for p-type $CuInTe_2$ and $AgInTe_2$ increases monotonically with the carrier concentration (Fig. 6a and c), ZT for n-type $AgInTe_2$ presents a maximum between $n = 2.5 \times 10^{18}$ and 5×10^{18} cm^{-3} (Fig. 6e), which is connected to its PF as was described above. These results cannot be compared with experimental values because, although experimental ZT values are reported at specific temperatures, it is not common that the carrier concentration of the samples are measured beyond 300 K. Cao *et al.* found that the carrier concentration of $CuInTe_2$ at 600 K is close to 10^{19} cm^{-3} so it can be assumed that $n > 10^{19}$ cm^{-3} at 700 K. Our predictions for $CuInTe_2$ show ZT values between 0.38 and 0.65 at 700 K and $n > 10^{19}$ cm^{-3} which is in very good agreement with experimental reports whose values range between 0.35 and 0.6. Similarly, Wang *et al.* reported a ZT of 0.18 at 700 K and $n = 3.4 \times 10^{18}$ cm^{-3} for $AgInTe_2$, which match well with our prediction of ZT = 0.24. Although the accuracy of the model is demonstrated, it is necessary to discuss if the optimized parameters are accessible from an experimental point of view. Controlling experimentally the carrier concentration to optimize the TE performance of materials is not a trivial task. In addition to the study presented in this work, an accurate thermodynamic analysis to define the dopability window of the material should be performed to establish whether the optimal conditions can be experimentally achieved. Recently, Adamczyk *et al.* have explored the dopability of $CuInTe_2$ (ref. 57) and $AgInTe_2$.[58] This information is particularly critical for $AgInTe_2$ because previous experimental work had reported very low carrier concentration, well below the optimal calculated concentrations which are above 10^{19} cm^{-3} at 700 K. Promisingly, Adamczyk *et al.* found p-type $AgInTe_2$ samples with carrier concentrations around 10^{18} cm^{-3} at 323 K which were synthesized at In- and Te-rich conditions. These results suggest that it might be possible to achieve carrier concentrations near the optimal value above 10^{19} cm^{-3} at 700 K for p-type $AgInTe_2$ in order to maximize ZT.

To the best of our knowledge, most previous experimental work refers to polycrystalline samples, where grains are in the range of several micrometers, so ZT is barely affected by their size. Nanostructuring effects on ZT were explored at 700 K for both materials. Overall, reducing the grain size at nanoscale drastically improves the TE performance of $CuInTe_2$ and $AgInTe_2$

(Fig. 6b, d and f). For instance, ZT for p-type $CuInTe_2$ is increased from 0.53 to 0.73 when grain size is around 100 nm and $n = 4.5 \times 10^{19}$ cm^{-3} (Fig. 6b). This performance can be surpassed if the average size of the crystal is in the range of 10–20 nm, where ZT = 1.28. Using the same carrier concentration, ZT for p-type $AgInTe_2$ goes from 0.99 to 1.24 or 1.98 when grain size are 100 and 10 nm, respectively (Fig. 6d). Despite of the moderate TE performance of n-type $AgInTe_2$, its ZT is also improved around 50% when grain is reduced around 10 nm from ZT = 0.38 to 0.55 at their optimal carrier concentration (Fig. 6f).

4 Conclusions

Nanostructuring is a solid tool for the improvement and optimization of the TE performance of materials. Despite the advent of high-throughput experimental techniques, the synthesis, characterisation and property measurement of samples in which ZT depends on many variables do not represent a time and cost efficient solution to lead this strategy. The combination of new *ab initio* methodologies to predict transport properties with machine learning[59] and high-throughput frameworks establishes a solid foundation for the accurate prediction of ZT and its optimization based on temperature, carrier concentration and crystal grain size. In this work, the transport properties and TE performance of $CuInTe_2$ and $AgInTe_2$ have been charted. Our results accurately predict S, σ, κ_{latt}, PF, and ZT for both materials, with very good agreement with previous experimental reports. It is confirmed that the largest PF experimentally found for $CuInTe_2$ with respect to $AgInTe_2$ is due to the lower carrier concentration in the $AgInTe_2$ samples. p-type $AgInTe_2$ presents a PF almost as high as $CuInTe_2$ when they are compared at the same temperature and especially same carrier concentration. This high PF united to its extremely low κ_{latt} makes p-type $AgInTe_2$ a good TE candidate (ZT = 0.99). Nanostructuring improves the TE performance of all explored materials. Computing the electrons–holes and phonons mean free path is the key to understand this behavior. The almost two order of magnitude difference between the electron and phonons MFP opens a window in which κ_{latt} is reduced but PF is mostly unaltered. ZT at 700 K is improved by factor of 2.6 and 2 with grain sizes between 10 and 20 nm for $CuInTe_2$ and $AgInTe_2$, respectively. While the improvement factor at this temperature is higher for $CuInTe_2$ than for $AgInTe_2$, the latter is improved starting from a substantially higher bulk ZT. It is particularly interesting that our simulations predict that p-type $AgInTe_2$ could reach ZT $\approx$ 2 at 700 K if its carrier concentration is tuned and the samples are nanostructured to around 10 nm grain size. These results validate and encourage the use of high-throughput computational approaches to accelerate the discovery and optimization of new and more efficient TE materials.

Author contributions

The authors confirm contribution to the paper as follows: conceptualization: J. J. P., R. G. C. and A. M. M.; data curation: E. J. B. and V. P.; investigation: E. J. B, V. P. and J. J. P.;

16740 | *J. Mater. Chem. A*, 2023, **11**, 16734–16742

This journal is © The Royal Society of Chemistry 2023

References

1 R. Freer, D. Ekren, T. Ghosh, K. Biswas, P. Qiu, S. Wan, L. Chen, S. Han, C. Fu, T. Zhu, A. K. M. A. Shawon, A. Zevalkink, K. Imasato, G. J. Snyder, M. Ozen, K. Saglik, U. Aydemir, R. Cardoso-Gil, E. Svanidze, R. Funahashi, A. V. Powell, S. Mukherjee, S. Tippireddy, P. Vaqueiro, F. Gascoin, T. Kyratsi, P. Sauerschnig and T. Mori, *J. Phys. Energy*, 2022, **4**, 022002.

2 T. Zhu, Y. Liu, C. Fu, J. P. Heremans, J. G. Snyder and X. Zhao, *Adv. Mater.*, 2017, **29**, 1605884.

3 A. Ganose, J. Park, A. Faghaninia, R. Woods-Robinson, K. Persson and A. Jain, *Nat. Commun.*, 2021, **12**, 2222.

4 J. J. Plata, P. Nath, D. Usanmaz, J. Carrete, C. Toher, M. de Jong, M. D. Asta, M. Fornari, M. Buongiorno Nardelli and S. Curtarolo, *npj Comput. Mater.*, 2017, **3**, 45.

5 W. Rahim, J. M. Skelton and D. O. Scanlon, *J. Mater. Chem. A*, 2021, **9**, 20417–20435.

6 K. B. Spooner, A. M. Ganose and D. O. Scanlon, *J. Mater. Chem. A*, 2020, **8**, 11948–11957.

7 J. J. Plata, P. Nath, J. F. Sanz and A. Márquez, in *Comprehensive Inorganic Chemistry III*, ed. J. Reedijk and K. R. Poeppelmeier, Elsevier, 3rd edn, 2023, pp. 446–460.

8 E. J. Blancas, J. J. Plata, J. Santana, F. Lemus-Prieto, A. M. Márquez and J. F. Sanz, *J. Mater. Chem. A*, 2022, **10**, 19941–19952.

9 R. Li, X. Li, L. Xi, J. Yang, D. Singh and W. Zhang, *ACS Appl. Mater. Interfaces*, 2019, **11**, 24859–24866.

10 T. J. Slade, T. P. Bailey, J. A. Grovogui, X. Hua, X. Zhang, J. J. Kuo, I. Hadar, G. J. Snyder, C. Wolverton, V. P. Dravid, C. Uher and M. G. Kanatzidis, *Adv. Energy Mater.*, 2019, **9**, 1901377.

11 Y. Yu, C. Zhou, X. Zhang, L. Abdellaoui, C. Doberstein, B. Berkels, B. Ge, G. Qiao, C. Scheu, M. Wuttig, O. Cojocaru-Miredin and S. Zhang, *Nano Energy*, 2022, **101**, 107576.

12 J.-Y. Hwang, J. Kim, H.-S. Kim, S.-I. Kim, K. H. Lee and S. W. Kim, *Adv. Energy Mater.*, 2018, **8**, 1800065.

13 X. Zhang, B. Zhang, K.-l. Peng, X.-c. Shen, G.-t. Wu, Y.-c. Yan, S.-j. Luo, X. Lu, G.-y. Wang, H.-s. Gu and X.-y. Zhou, *Nano Energy*, 2018, **43**, 159–167.

14 S. Hu, W. Han, X. Li, M. Ye, Y. Lu, C. Jin, Q. Liu, J. Wang, J. He, C. Cazorla, Y. Zhu and L. Chen, *Adv. Energy Mater.*, 2022, **12**, 2201469.

15 L. Hicks and M. Dresselhaus, *Phys. Rev. B: Condens. Matter Mater. Phys.*, 1993, **47**, 16631–16634.

16 X. Yan, G. Joshi, W. Liu, Y. Lan, H. Wang, S. Lee, J. Simonson, S. Poon, T. Tritt, G. Chen and Z. Ren, *Nano Lett.*, 2011, **11**, 556–560.

17 S. He, S. Lehmann, A. Bahrami and K. Nielsch, *Adv. Energy Mater.*, 2021, **11**, 2101877.

18 J. Makongo, D. Misra, X. Zhou, A. Pant, M. Shabetai, X. Su, C. Uher, K. Stokes and P. Poudeu, *J. Am. Chem. Soc.*, 2011, **133**, 18843–18852.

19 M. G. Kanatzidis, *Chem. Mater.*, 2010, **22**, 648–659.

20 J. J. Plata, V. Posligua, A. M. Márquez, J. F. Sanz and R. Grau-Crespo, *Chem. Mater.*, 2022, **34**, 2833–2841.

21 J. Zhang, L. Huang, C. Zhu, C. Zhou, B. Jabar, J. Li, X. Zhu, L. Wang, C. Song, H. Xin, D. Li and X. Qin, *Adv. Mater.*, 2019, **31**, 1905210.

22 T. Ren, Z. Han, P. Ying, X. Li, X. Li, X. Lin, D. Sarker and J. Cui, *ACS Appl. Mater. Interfaces*, 2019, **11**, 32192–32199.

23 G. Kresse and J. Hafner, *Phys. Rev. B: Condens. Matter Mater. Phys.*, 1993, **47**, 558–561.

24 G. Kresse and J. Furthmüller, *Phys. Rev. B: Condens. Matter Mater. Phys.*, 1996, **54**, 11169–11186.

25 P. E. Blöchl, *Phys. Rev. B: Condens. Matter Mater. Phys.*, 1994, **50**, 17953–17979.

26 J. P. Perdew, K. Burke and M. Ernzerhof, *Phys. Rev. Lett.*, 1996, **77**, 3865–3868.

27 S. Grimme, J. Antony, S. Ehrlich and H. Krieg, *J. Chem. Phys.*, 2010, **132**, 154104.

28 C. E. Calderon, J. J. Plata, C. Toher, C. Oses, O. Levy, M. Fornari, A. Natan, M. J. Mehl, G. L. W. Hart, M. Buongiorno Nardelli and S. Curtarolo, *Comput. Mater. Sci.*, 2015, **108**, 233–238.

29 F. Eriksson, E. Fransson and P. Erhart, *Adv. Theory Simul.*, 2019, **2**, 1800184.

30 E. Fransson, F. Eriksson and P. Erhart, *npj Comput. Mater.*, 2020, **6**, 135.

31 W. Li, J. Carrete, N. A. Katcho and N. Mingo, *Comput. Phys. Commun.*, 2014, **185**, 1747–1758.

32 J. Heyd, G. E. Scuseria and M. Ernzerhof, *J. Chem. Phys.*, 2003, **118**, 8207–8215.

33 A. V. Krukau, O. A. Vydrov, A. F. Izmaylov and G. E. Scuseria, *J. Chem. Phys.*, 2006, **125**, 224106.

34 S. Baroni and R. Resta, *Phys. Rev. B: Condens. Matter Mater. Phys.*, 1986, **33**, 7017–7021.

35 M. Gajdoš, K. Hummer, G. Kresse, J. Furthmüller and F. Bechstedt, *Phys. Rev. B: Condens. Matter Mater. Phys.*, 2006, **73**, 045112.

This journal is © The Royal Society of Chemistry 2023

J. Mater. Chem. A, 2023, **11**, 16734–16742 | **16741**

36 G. D. Holah, A. A. Schenk, S. Perkowitz and R. D. Tomlinson, *Phys. Rev. B: Condens. Matter Mater. Phys.*, 1981, **23**, 6288–6293.

37 V. Kumar, *J. Phys. Chem. Solids*, 1987, **48**, 827–831.

38 Y. Zhou, X. Li, L. Xi and J. Yang, *J. Materiomics*, 2021, **7**, 19–24.

39 B. Kuhn, W. Kaefer, K. Fess, K. Friemelt, C. Turner, M. Wendl and E. Bucher, *Phys. Status Solidi A*, 1997, **162**, 661–671.

40 P. Prabukanthan and R. Dhanasekaran, *Mater. Res. Bull.*, 2008, **43**, 1996–2004.

41 R. Liu, L. Xi, H. Liu, X. Shi, R. Liu and L. Chen, *Chem. Comm.*, 2012, **48**, 3818–3820.

42 Y. Luo, J. Yang, Q. Jiang, W. Li, D. Zhang, Z. Zhou, Y. Cheng, Y. Ren and X. He, *Adv. Energy Mater.*, 2016, **6**, 1600007.

43 Z. Xia, G. Wang, X. Zhou and W. Wen, *Mater. Res. Bull.*, 2018, **101**, 184–189.

44 H. Yu, L.-C. Chen, H.-J. Pang, X.-Y. Qin, P.-F. Qiu, X. Shi, L.-D. Chen and X.-J. Chen, *Mater. Today Phys.*, 2018, **5**, 1–6.

45 Y. Yan, X. Lu, G. Wang and X. Zhou, *ACS Appl. Energy Mater.*, 2020, **3**, 2039–2048.

46 C. Wang, Q. Ma, H. Xue, Q. Wang, P. Luo, J. Yang, W. Zhang and J. Luo, *ACS Appl. Energy Mater.*, 2020, **3**, 11015–11023.

47 Y. Cao, X. Su, F. Meng, T. Bailey, J. Zhao, H. Xie, J. He, C. Uher and X. Tang, *Adv. Funct. Mater.*, 2020, **30**, 2005861.

48 Q. Xiong, Y. Yan, N. Li, B. Zhang, S. Zheng, Y. Feng, G. Wang, H. Liao, Z. Huang, J. Li, G. Wang, X. Lu and X. Zhou, *Appl. Phys. Lett.*, 2022, **121**, 013903.

49 J. Mackey, F. Dynys and A. Sehirlioglu, *Rev. Sci. Instrum.*, 2014, **85**, 085119.

50 J. Wei, H. Liu, L. Cheng, J. Zhang, J. Liang, P. Jiang, D. Fan and J. Shi, *AIP Adv.*, 2015, **5**, 107230.

51 Y. Zhong, Y. Luo, X. Li and J. Cui, *Sci. Rep.*, 2019, **9**, 18879.

52 G. Zhou and D. Wang, *Phys. Chem. Chem. Phys.*, 2016, **18**, 5925–5931.

53 R. Liu, Y. Qin, N. Cheng, J. Zhang, X. Shi, Y. Grin and L. Chen, *Inorg. Chem. Front.*, 2016, **3**, 1167–1177.

54 H. Xie, S. Hao, S. Cai, T. P. Bailey, C. Uher, C. Wolverton, V. P. Dravid and M. G. Kanatzidis, *Energy Environ. Sci.*, 2020, **13**, 3693–3705.

55 Y. Li, J. Liu and J. Hong, *Phys. Rev. B*, 2022, **106**, 094317.

56 H. Yu, L.-C. Chen, H.-J. Pang, P.-F. Qiu, Q. Peng and X.-J. Chen, *Phys. Rev. B*, 2022, **105**, 245204.

57 J. M. Adamczyk, L. C. Gomes, J. Qu, G. A. Rome, S. M. Baumann, E. Ertekin and E. S. Toberer, *Chem. Mater.*, 2021, **33**, 359–369.

58 V. Meschke, L. C. Gomes, J. M. Adamczyk, K. M. Ciesielski, C. M. Crawford, H. Vinton, E. Ertekin and E. S. Toberer, *J. Mater. Chem. C*, 2023, **11**, 3832–3840.

59 L. M. Antunes, Vikram, J. J. Plata, A. V. Powell, K. T. Butler and R. Grau-Crespo, in *Machine Learning Approaches for Accelerating the Discovery of Thermoelectric Materials*, ACS, 2022, ch. 1, pp. 1–32.

16742 | *J. Mater. Chem. A*, 2023, **11**, 16734–16742

This journal is © The Royal Society of Chemistry 2023